High-Efficiency Generation-Collection Microelectrochemical Platform for Interrogating Electroactive Thin Films

Morgan J. Anderson and Richard M. Crooks*

Department of Chemistry, Center for Nano- and Molecular Science and Technology, and the Center for Electrochemistry, The University of Texas at Austin, 105 East 24th Street, Stop A5300, Austin, Texas 78712-1224, United States

S *Supporting Information*

ABSTRACT: Here we report on the development of a high-efficiency, dual channel-electrode (DCE) generation-collection system and its application for interrogating redox-active surface-adsorbed thin films. DCE systems consist of two electrodes configured on the base of a microfluidic channel. Under laminar flow conditions, a redox reaction can be driven on the upstream generator electrode, and the products carried by convection to the downstream collector electrode where the reverse redox reaction occurs. One significant outcome of this report is that simple fabrication techniques can be used to prepare DCE systems that have collection efficiencies of up to 97%. This level of efficiency makes it possible to quantitatively measure the charge associated with redox-active thin films interposed between the generator and collector electrodes. This is important, because it provides a means for interrogating species that are not in sufficiently close proximity to an electrode to enable direct electron transfer or electroactive films adsorbed to insulating surfaces. Here, the method is demonstrated by comparing results from this indirect surface interrogation method, using $Fe(CN)_6^{3-}$ as the redox probe, and direct electroreduction of Au oxide thin films. These experimental results are further compared to finite-element simulations.
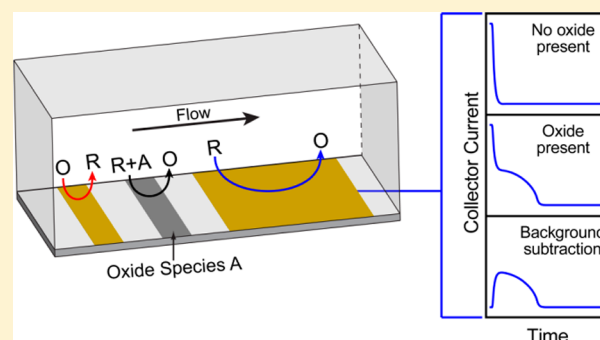
Here, we report on the development of a high-efficiency, dual channel-electrode (DCE) generation-collection system, and its application for the interrogation of electrochemically active surface-adsorbed species. DCE systems consist of two electrodes configured on the base of a microfluidic channel. Under flow conditions, an electrochemical reaction can be driven on the upstream generator electrode and the reactants carried by convection to the downstream collector electrode where the reverse reaction occurs (Scheme 1a). One significant outcome of this report is that simple fabrication techniques can be used to prepare DCE systems that have collection efficiencies of up to 97%. This level of efficiency makes it possible to quantitatively measure electrochemically active thin films interposed between the generator and collector electrodes (Scheme 1b). This is important for interrogating redox species that are not in sufficiently close proximity to an electrode to enable direct electron transfer and for measuring thin films adsorbed to insulating surfaces. Examples might include thick self-assembled monolayers, bilayer membranes incorporating redox-active proteins, or, as shown here, redox-active metal oxide thin films.

Experimental and computational characteristics of DCE systems have been described previously.[1−4] In these systems, two parallel, coplanar metal electrodes are situated on the floor of a rectangular channel, and solution flow is initiated under laminar conditions. The upstream generator electrode is held at a potential, E^{gen}, that is sufficient to initiate a redox reaction of a solution-phase species (O + ne^- → R in Scheme 1). The product of this reaction is carried to the downstream collector electrode, which is held at a potential, E^{col}, that is sufficient to drive the reverse reaction (R → O + ne^-). The most important parameter of DCE systems, like any generation-collection system, is the collection efficiency (N) defined by eq 1.

$$N = -\frac{i^{col}}{i^{gen}} \tag{1}$$

Here, i^{gen} and i^{col} are the currents at the generator and collector electrodes, respectively. All values of N discussed hereafter are derived from the mass-transfer limited currents at the generator and collector electrodes (i_L^{gen} and i_L^{col}, respectively).

DCEs have a wide range of uses, including: investigation of homogeneous reaction kinetics,[3,5,6] evaluation of catalysts,[7,8] study of corrosion,[9−14] and in situ study of flow in microchannels.[15−18] DCE methods have not become as popular as the other two principal methods for carrying out electrochemical generation-collection studies: rotating ring disk voltammetry (RRDV)[19] and generation-collection scanning electrochemical microscopy (gc-SECM).[20] This is likely a

Scheme 1
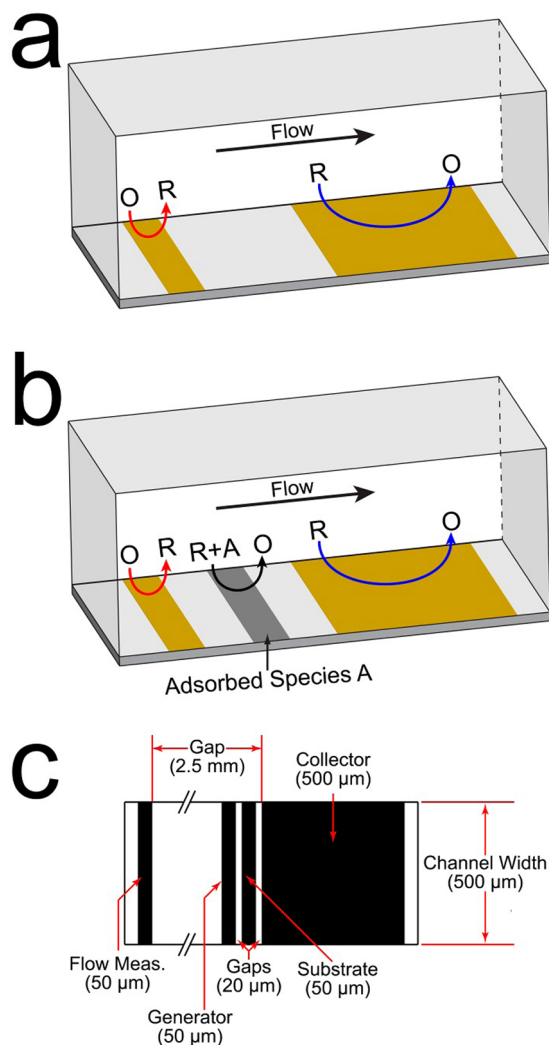
consequence of perceived difficulties with device fabrication, initiating a well-defined, stable hydrodynamic flow, and limited collection efficiencies (25−40% is typical).[8,10,11]

Advances in simple microfabrication methods have, to a large extent, ameliorated fabrication difficulties. Soft lithography,[21−23] in particular, has greatly expanded the range of microdevice methodologies available to electrochemists. Recent examples of very high collection efficiencies reported by us (97%)[7] and others (78%)[24] have further expanded the scope of DCE methods. Finally, the increasing popularity of microelectrochemical methods encourages development of novel, in situ methods of detection. For example, the Bard group developed a technique called surface interrogation SECM (si-SECM), which has a very high collection efficiency (~100%),[25,26] for studying the properties of thin films in standard electrochemical cells. They used si-SECM to study oxides on Pt and Au,[27,28] decomposition of formic acid on Pt,[29] and photoelectrogenerated hydroxyl radicals on TiO$_2$ and W/Mo-BiVO$_4$.[30,31] Our goal here is to show that similar types of experiments can be carried out in the microfluidic format without the need for complex and expensive instrumentation.

In the present article, we describe the fabrication of simple microelectrochemical devices, capable of very high collection efficiencies, and their use for probing the electrochemical properties of a model surface: an oxide layer on Au. The importance of key parameters, including electrode configuration and flow rate, are discussed in detail. Finally, the experimental results are correlated to finite element simulations.

■ EXPERIMENTAL SECTION

Chemicals and Materials. All solutions were prepared using Milli-Q water (18.2 Ω·cm). 1,1′-Ferrocenedimethanol (FcDM, 97%, Sigma-Aldrich), K$_3$Fe(CN)$_6$ (99+%, Acros Organics), KNO$_3$ (primary nitrogen standard, Fisher Scientific), KH$_2$PO$_4$ (ACS grade, EM Science), and K$_2$HPO$_4$ (ACS grade, EM Science) were used as received.

Glass slides coated with a 100 nm thick Au film (no adhesion layer) were purchased from Evaporated Metal Films (Ithaca, NY). AZP 4620 photoresist and AZ 421k developer were purchased from AZ Electronic Materials. SU-8 2025 photoresist was purchased from MicroChem. Sylgard 184 poly-(dimethylsiloxane) (PDMS) kits were purchased from Fisher Scientific.

Instrumentation. Electrochemistry was performed using a CH Instruments (Austin, TX) Model 700D or 700E bipotentiostat equipped with a Faraday cage. All electrochemical experiments were performed in the four-electrode bipotentiostat configuration using a Hg/Hg$_2$SO$_4$ reference electrode and a Pt wire counter electrode. Flow was introduced using a Pico Pump 11 Elite syringe pump from Harvard Apparatus (Holliston, MA) and 50 and 500 μL luer-lock gastight syringes from Hamilton (Reno, NV). Syringes were connected to the microfluidic device using PEEK tubing and fittings from IDEX Health and Science (Oak Harbor, WA). Glass/PDMS devices were fabricated by standard photo-patterning techniques (see Supporting Information).[22] A scaled representation of the electrode pattern is provided in Scheme 1c, and a summary of the average feature dimensions, measured by optical microscopy, is included in Supporting Information Table S1.

Microelectrochemical Measurements. Bubbles anywhere in the flow path created significant fluctuations in flow rate and noise in current transients. To remove bubbles from the flow path, two syringes, 50 (1.03 mm ID) and 500 μL (3.26 mm ID), were connected to a two-way switching valve. This allowed flow from one of the two syringes to reach the channel, while the other was directed to a reagent reservoir, allowing the syringes to be refilled without being disconnected and thereby reducing the likelihood of bubbles entering the flow line. The cross-sectional areas of the inner syringe barrels are such that switching between the two results in a 10-fold change in the volumetric flow rate through the channel. Consequently, measurements could be made with the 50 μL syringe, providing a stable flow profile at low flow rates, while bubbles could easily be purged with the 500 μL syringe. A schematic representation of the flow system, as well as a photograph, are shown in Figure S1 in the Supporting Information.

Prior to attaching the syringes to the system, the tubing assembly was flushed with copious amounts of water, as well as several aliquots of the redox solution, to remove possible contaminants. Contact to the electrodes was made via Cu tape, which was clamped to the contact pads of the electrodes to ensure reliable electrical connections. The clamp incorporated electrical wires that were connected to a four-way electronically actuated switch to allow quick switching between electrodes.

The fluidic system is fully described in the Supporting Information. Briefly, however, it consisted of a PDMS monolith, having a 6 mm long channel and 1.20 mm and 8.00 mm-diameter inlet and outlet reservoirs, respectively, punched at each end. After mating the PDMS block to the glass/electrode assembly, a conical adapter was used as an interface between the tubing from the two-way valve and the inlet reservoir. A Hg/Hg_2SO_4 reference electrode and Pt wire counter electrode were inserted into the outlet reservoir. The channel was then purged at a volumetric flow rate of 75 μL min^{-1} to remove any bubbles from the flow path. Prior to collecting data, the flow rate was allowed to equilibrate for at least 5 min. Uncompensated resistance within the micro-electrochemical cell was measured to be 4.5 $\pm$ 0.4 kΩ for the generator electrode.

Finite Element Simulations. Modeling was performed with the COMSOL, version 4.3b, commercial package using a Dell Precision T7500 workstation equipped with dual six core Intel Xeon Processors (2.40 GHz) and 24GB of RAM.

Simulations were performed in 2D, independently solving for fluid dynamics and mass transport of analyte. Fluid dynamics modeling assumed laminar flow and a steady-state (i.e., a fully developed) flow profile. For both steady-state and transient calculations of mass transport, Butler−Volmer kinetics were used to describe the flux of molecules at the surface of the electrode. Complete details of the numerical models are available in the Supporting Information.

■ RESULTS AND DISCUSSION

Flow-Rate Measurement. Quantitative analysis of the electrochemical data discussed in this article requires precise knowledge of flow rate. Accordingly, flow rates were measured using slight variations to a previously described electrochemical method.[15,32,33] First, the microchannel was filled with 0.50 mM FcDM in 0.10 M KNO_3. Next, at $t = 0$, a potential step was applied to a flow-measurement electrode, fabricated for this purpose and situated 2.5 mm upstream from the collector electrode of each device (Scheme 1c), to convert FcDM to FcDM$^+$ at the mass-transfer-limited rate. The time between the potential step at the flow measurement electrode and the initial increase or decrease in the collector current (i^{col}), which we call the critical time (t_{crit}), corresponds to the average linear flow rate within the channel. The volumetric flow rate (Q) can then be determined using eq 2.

$$Q = \gamma \frac{hwg}{t_{crit}} \qquad (2)$$

Here, γ is a dimensionless geometrical factor,[15] which is taken to be equal to 1 in this instance, h is the channel height, w is the channel width, and g is the distance between the flow measurement electrode and collector.

As shown graphically in Figure S2 in the Supporting Information, the value of t_{crit} was determined by taking the derivative of the i^{col} transient ($\Delta i^{col}/\Delta t$) to more accurately determine its location. Then a threshold value of $\Delta i^{col}/\Delta t$ (φ) was established according to eq 3.

$$\varphi = \bar{x}_b \pm 10 s_b \qquad (3)$$

Here, $\bar{x}_b$ and s_b are the average and standard deviation of the baseline values of $\Delta i^{col}/\Delta t$, respectively. The value of t_{crit} was defined as the time when the derivative rose above or fell below φ.
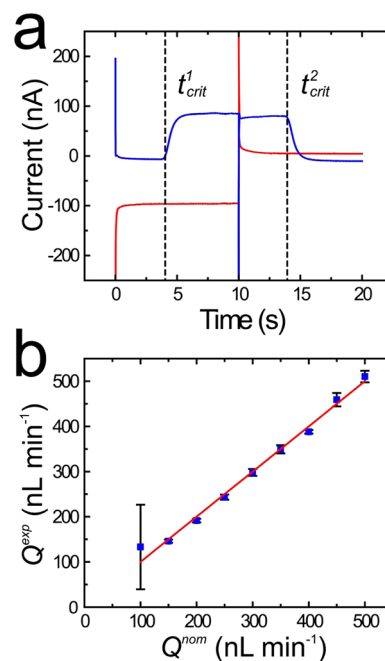
Figure 1. (a) Plot of current as a function of time used for measuring flow rate in the microelectrochemical device. A solution containing 0.50 mM FcDM and 0.10 M KNO_3 flowed in the channel at a nominal volumetric flow rate of 300 nL min^{-1}. The flow measurement electrode was stepped from −0.35 to 0.20 V for 10.0 s, and then back to −0.35 V vs MSE for 10.0 s. The collector electrode was located 2.5 mm downstream and was held at a constant potential of −0.35 V throughout the experiment. The current responses of the flow measurement (red lines) and collector (blue lines) electrodes are shown. The time delay between the potential step at the generator electrode and the initial increase (t_{crit}^1) or decrease (t_{crit}^2) in the collector current is denoted by dashed black lines. An explanation of how the t_{crit} values were determined is provided in the Supporting Information. (b) Comparison of the experimental (Q^{exp}) and nominal (Q^{nom}) flow rates. The red line has a slope of 1 and represents perfect correspondence.

A generation-collection experiment was then performed by pulsing E^{gen} 10 times between −0.35 and 0.20 V, while E^{col} was held constant at −0.35 V. Figure 1a shows the transients of i^{gen} (red) and i^{col} (blue) resulting from the first two steps of this amperometric experiment. The vertical dashed lines correlate to the initial increase (t_{crit}^1) and decrease (t_{crit}^2) in current, as determined by the method discussed earlier. Good agreement is observed between t_{crit}^1 (4.04 s) and t_{crit}^2 (3.94 s).

Figure 1b shows the correlation between the experimentally measured value of the volumetric flow rate (Q^{exp}) and the nominal value (Q^{nom}) set at the pump. Each data point in this plot represents 16 measurements performed using the same microelectrochemical device, and the red line represents the condition $Q^{exp} = Q^{nom}$ (slope =1). Clearly, the flow-rate measurement method is highly reproducible and there is excellent agreement between the measured and nominal flow rates. These types of measurements are important, because accurate correlation of N and surface-titration current transients to finite-element simulations require that Q be predictable and stable.

Characterization of a High-Efficiency DCE Configuration. Comprehensive studies of the various electrochemical mass-transfer regimes within microfluidic devices have been elucidated by Amatore and co-workers.[4,34] On the basis of the

geometric parameters of the channel, electrode dimensions, and analyte diffusivity, a broad range of behavior can be observed. Most channel electrode systems operate in the high mass transfer, or "Levich", regime where the mass-transfer-limited current, i_L, is proportional to $Q^{1/3}$, and the diffusion layer is thin relative to the height of the channel.[3] However, it is also possible to operate in low mass-transfer thin-layer regimes, where the concentration of reactants is fully depleted throughout the height of the channel, and pseudo-thin-layer regimes, where the concentration is partially depleted throughout the height of the channel.[34] These regimes can be accessed by decreasing the linear flow rate of the solution and ensuring that the height of the channel is shallow (15−20 μm), effectively increasing the time redox molecules spend over the electrode before passing it. High collection efficiencies are obtained by ensuring that the collector electrode operates in a thin-layer regime. However, for pseudothin-layer regimes, such as that at the generator electrode in our experiments, there are no analytical solutions for predicting i_L on the basis of experimental parameters. Accordingly, experimental results may only be compared to finite-element simulations.

The performance of the high-efficiency DCE configuration, illustrated in Scheme 1a, was evaluated by chronoamperometry. Figure 2a shows representative chronoamperograms obtained in a solution containing 0.53 mM FcDM and 0.10 M KNO$_3$. Here, w was 496.7 μm and h was 16.0 μm. The generator length was 44.3 μm and the collector length was 498.9 μm with a 96.5 μm gap between them. While holding E^{col} constant at −0.35 V, E^{gen} was stepped from −0.35 to 0.20 V and held for 5.0 s, allowing i^{gen} to stabilize at the mass-transfer-limited value after a brief charging period. The value of i^{col} increases from the baseline until it also reaches a mass-transfer-limited value. Next, E^{gen} was stepped back to −0.35 V and held for 5.0 s and i^{gen} and i^{col} are observed to quickly decay to their baseline values. The values of i_L^{gen} and i_L^{col} were determined by baseline subtraction. The measurements shown were obtained at Q = 200, 300, 400, and 500 nL min^{-1}. The trace at 200 nL min^{-1} reveals a significant variation in i_L^{gen} (red) and i_L^{col} (blue) as a function of time. This variation is representative of all scans obtained using flow rates between 100 and 250 nL min^{-1}, and likely arises from an instability in the flow profile due to either the syringe pump stepping motor or natural convection. Above 250 nL min^{-1}, i^{gen} and i^{col} are quite stable.

Figure 2b shows the values of i_L^{gen} (red squares) and i_L^{col} (blue circles) as a function of Q along with simulated results (black line). All measurements were performed on the same device and each point represents five separate measurements. At low values of Q, the variation in the measurements of i_L^{gen} are noticeable (RSD = 0.09 at Q = 150 nL min^{-1}) but at higher values the error is very small (RSD = 0.005 at Q = 550 nL min^{-1}). The measured uncertainty in i_L^{col} is similar to that of i_L^{gen}. This deviation suggests that measurements at low Q are less reproducible as discussed earlier.

The simulated values of i_L^{gen} are in good agreement with the experimental values, but the simulated values of i_L^{col} are consistently higher than those obtained from the experiments. This is a consequence of the large size of the collector electrode and corresponding difficulty of simulating it with a sufficiently dense mesh. It is well-known that increasing the mesh density results in lower values of i_L^{col} which converge onto the exact solution.[35] However, this is beyond our current capability as current models fully consume the available computational resources. On the basis of eq 1, we expect discrepancies
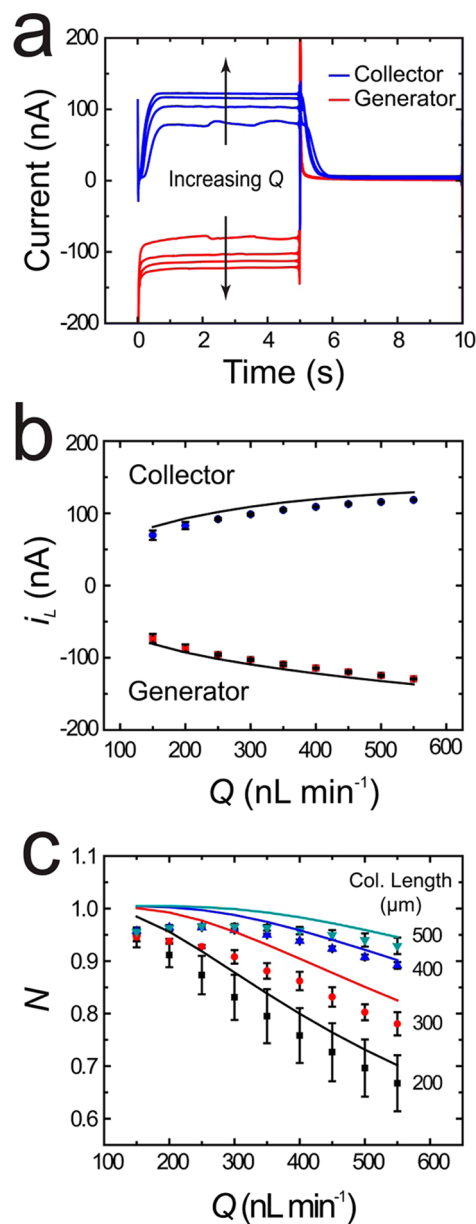
Figure 2. (a) Chronoamperograms obtained as a function of flow rate (Q = 200, 300, 400, and 500 nL min^{-1}). The solution contained 0.53 mM FcDM and 0.10 M KNO$_3$, and the microelectrochemical device had a nominal collector length of 500 μm. The generator electrode was stepped from −0.35 to 0.20 V for 5.0 s and then back to −0.35 V for 5.0 s. The collector electrode was held at a constant potential of −0.35 V for the entire measurement. The current response of the generator electrode (red lines) and collector electrode (blue lines) are shown. (b) Plot of limiting currents at the generator and collector electrodes as a function of Q. Each point represents the average of five measurements performed using a single microelectrochemical device. The solid lines represent simulated results. The nominal collector length was 500 μm. (c) Plot of collection efficiency (N) as a function of Q. The nominal lengths of the collector electrodes were 200 (black squares), 300 (red circles), 400 (blue triangles), and 500 μm (green triangles). Each point represents the average value of N obtained using three different microelectrochemical devices. The solid lines represent simulated results.

between experimental and simulated values of i_L^{col} to be reflected in N.

Figure 2c shows a plot of N versus Q obtained using microelectrochemical devices having nominal collector electrode lengths of 200 (black squares), 300 (red circles), 400 (blue triangles), and 500 μm (green triangles). Here, each data set was obtained using three different devices and each point represents the average of five measurements from each of these devices. For devices having 200 and 300 μm-long collector electrodes, the collection efficiencies are ~0.95 at Q = 150 nL min^{-1}. At higher values of Q, N decreases, which is consistent with the trends described by Amatore et al.[34] Devices having collector electrodes with nominal lengths of 400 and 500 μm also have values of N = ~0.95 at Q = 150 nL min^{-1}, but the collection efficiency initially increases as Q increases from 150 to 250 nL min^{-1}. This initial increase in N likely arises from an instability of the flow profile, as discussed earlier. As Q is increased beyond 250 nL min^{-1}, N gradually decreases for all electrode lengths.

Surface Titrations of Gold Oxide Thin Films. To test the effectiveness of these microelectrochemical devices for measuring the electrochemical properties of thin films, we carried out surface redox titrations of electrochemically generated thin films of gold oxide. The titrations were performed using 1.0 mM $Fe(CN)_6^{3-}$ in 0.10 M pH 7.0 phosphate buffer. To ensure both high collection efficiencies and stable flow profiles, experiments discussed hereafter were performed using 500 μm-long collector electrodes and Q = 300 nL min^{-1}.

To ensure that the reducing power of $Fe(CN)_6^{4-}$ is sufficient to reduce gold oxide, we evaluate the electrochemical properties of each using the same type of microelectrochemical device used for the subsequent titration experiments. Figure 3a shows typical electrochemical behavior observed at a Au electrode having a nominal length of 50 μm. The black cyclic voltammogram was obtained as the potential was swept from −0.60 to 1.20 V and back again in a solution of pH 7.0 phosphate buffer. On the forward sweep, current due to the formation of gold oxide is observed at ~0.40 V. The oxide continues to grow slowly as the scan progresses, but at potentials above 1.00 V the current increases very rapidly due to the onset of water oxidation. On the return sweep, a peak due to reduction of the electrodeposited gold oxide is observed at 0.01 V. The red trace shows the reduction of $Fe(CN)_6^{3-}$ to $Fe(CN)_6^{4-}$ as the potential is swept from 0.20 V to −0.60 V. The sigmoidal shape of this curve indicates that convection is the dominant form of mass transport under these conditions. The half-wave potential is at −0.22 V, which is clearly sufficiently negative to reduce gold oxide.

The titration experiments were carried out as follows. First, a thin film of gold oxide was deposited onto the gold substrate electrode (Scheme 1) by sweeping its potential from −0.10 V to a preselected substrate deposition potential, E_{dep}^{sub}. Subsequently, two chronoamperograms were acquired with E^{gen} held at −0.50 V and E^{col} at 0 V. Figure 3b shows examples of the resulting i^{col} transients. The black trace represents the titration of the surface-adsorbed gold oxide electrodeposited at E_{dep}^{sub} = 0.80 V. For this experiment, $Fe(CN)_6^{3-}$ flows past the generator, where it is converted to $Fe(CN)_6^{4-}$. The $Fe(CN)_6^{4-}$ continues downstream until it encounters and reacts with the surface oxide present on the substrate electrode. Because this cross reaction results in conversion of $Fe(CN)_6^{4-}$ back to $Fe(CN)_6^{3-}$, the current detected at the collector electrode is lower than it would be in the absence of the oxide. This depletion of $Fe(CN)_6^{4-}$ continues until all of the oxide is
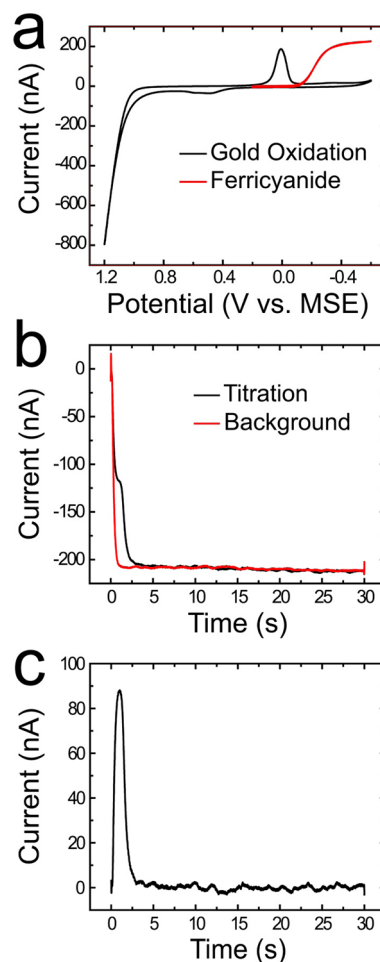
Figure 3. (a) Voltammetric responses obtained using a microelectrochemical device having a Au working electrode 50 μm in length. The black trace shows a typical response for deposition and subsequent reduction of gold oxide. The red trace corresponds to the reduction of 1.0 mM $Fe(CN)_6^{3-}$. All data were obtained using an electrolyte solution containing 0.10 M phosphate buffer (pH 7.0). The scan rate was 50 mV s^{-1} and the volumetric flow rate was 300 nL min^{-1}. (b) Chronoamperograms for a typical titration experiment. The black trace was obtained after electrodepositing gold oxide onto the substrate electrode using a linear sweep from −0.10 to 0.80 V at 50 mV s^{-1}. The generator electrode was stepped from 0 V to −0.50 V for 30.0 s while the collector electrode was held constant at 0 V for the duration of the experiment. The black trace is a typical collector response obtained during titration of a thin layer of gold oxide. The red trace is the background response when no oxide is present on the substrate electrode. Both traces were obtained in a solution containing 1.0 mM $K_3Fe(CN)_6$ and 0.10 M phosphate buffer (pH 7.0) flowing at 300 nL min^{-1} (c) The difference chronoamperogram obtained by subtracting the black and red traces in panel b.

consumed at the substrate electrode, after which time, i^{col} returns to its mass-transfer-limited value.

The second chronoamperogram (red trace) shown in Figure 3b was obtained under identical conditions as the first, but in this case no oxide was present between the generator and collector electrodes. Hence, the red trace is simply a background that is used to correct the black chronoamperogram for run-to-run fluctuations in flow rate or limiting current. Once obtained, the red and black scans are subtracted from one another and baseline corrected to yield the titration transient shown in Figure 3c. The integrated area under this curve

reveals the total amount of charge consumed by the cross reaction between $Fe(CN)_6^{4-}$ and the gold oxide thin film.

Figure 4a and 4b are examples of titration transients obtained for gold oxide thin films electrodeposited onto substrate
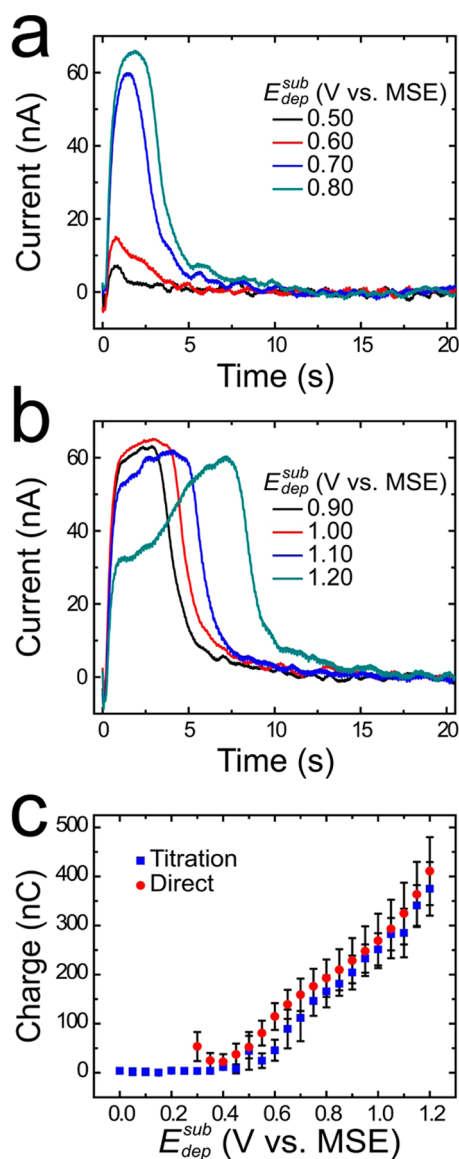
Figure 4. (a and b) Background-subtracted chronoamperograms for the titration of gold oxide as a function of the oxide deposition potential. The values of E_{dep}^{sub} are indicated in the legends. (c) Plot of integrated charge for the titration (blue squares) and direct electroreduction (red circles) of gold oxide as a function of E_{dep}^{sub}. Each data point represents the average of 2−3 independent experiments carried out using each of three different microelectrochemical devices. Experiments were performed using a solution containing 1.0 mM $K_3Fe(CN)_6$ and 0.10 M phosphate buffer (pH 7.0) flowing at $Q = 300$ nL min^{-1}. The nominal collector lengths were 500 μm.

electrodes using different values of E_{dep}^{sub}. These curves were manipulated in the same way as the one shown in Figure 3c. As E_{dep}^{sub} increases from 0.50 to 1.20 V, we anticipate electrodeposition of more oxide on the substrate electrode. These data bear that out: qualitatively, there is a rapid increase in the integrated area of the curves between 0.50 and 0.70 V, and then a more gradual increase between 0.70 and 1.10 V. At higher

values of E_{dep}^{sub} (1.20 V), the peak shape changes: the onset current evolves more slowly and the peak shifts to later times. The behavior at 1.20 V probably arises as a result of multiple oxide species forming on the surface, as discussed by Oesch and Janata.[36] In their study, oxides deposited at higher potentials required more negative potentials for electrochemical reduction. It follows that such oxides would also have different kinetic rate constants for the cross reaction with $Fe(CN)_6^{4-}$. A similar phenomenon is apparent in the si-SECM data reported by Rodríguez-López et al.[27]

The most convenient aspect of the gold/gold oxide system, and the reason we chose it for this study, is that the amount of oxide deposited on the substrate electrode at any given potential can be measured by direct electrochemical reduction. Figure 4c shows the relationship between the charge measured by surface titration (blue squares) and by direct electroreduction (red circles) as a function of the oxide deposition potential. Here, the direct electroreduction was performed using the same device after removal of $Fe(CN)_6^{3-}$. This is necessary, because the $Fe(CN)_6^{3-}$ reduction wave overlaps the oxide reduction peak. As shown in Figure 4c, titration and direct electroreduction methods yield very similar results, indicating that this surface titration method is suitable for measuring redox-active surface-adsorbed species.

Finite-Element Simulations. COMSOL software was used for the finite-element simulations, and a complete explanation of how these simulations were carried out, including the geometries used for modeling (Figures S3 and S4), is provided in the Supporting Information. Figure 5 compares typical experimental (black) and simulated (red) chronoamperograms. All the data shown in this figure were obtained using a single microelectrochemical device. The noise apparent in the experimental data arises from the syringe pump and the background subtraction process.

Qualitative inspection of these data leads to several conclusions regarding the interrogation of the adsorbed gold oxide. First, for low values of E_{dep}^{sub} (Figure 5a) there is poor agreement between the shapes of the experimental and simulated curves. This is probably a consequence of the small amount of adsorbed oxide generated in this potential range and the consequent uncertainty in the shape introduced during background subtraction. The results in Figure 5a are typical for charges < ~100 nC. At values of E_{dep}^{sub} above 0.60 V, such as for the data shown in Figure 5b and 5c, good agreement is observed between the shapes of experimental and simulated transients. However, once the deposition potential increases above 1.10 V, as shown for $E_{dep}^{sub} = 1.20$ V in Figure 5d, there is substantial deviation in the shapes of the experimental and simulated chronoamperograms. As mentioned earlier, this finding is probably because of the formation of multiple oxides, having correspondingly complex electrochemical properties, at extremely positive potentials.

■ SUMMARY AND CONCLUSIONS

We have shown that high collection efficiencies can easily and reproducibly be obtained using microelectrochemical devices in which the collector operates in a thin-layer electrochemical regime. Additionally, we used these high-efficiency systems to quantify surface adsorbed gold oxide in situ. An excellent correlation between the charges recorded for titration experiments and those measured by direct electrochemistry is observed. Under most conditions, the correspondence between the experimental results and finite-element simulations is also
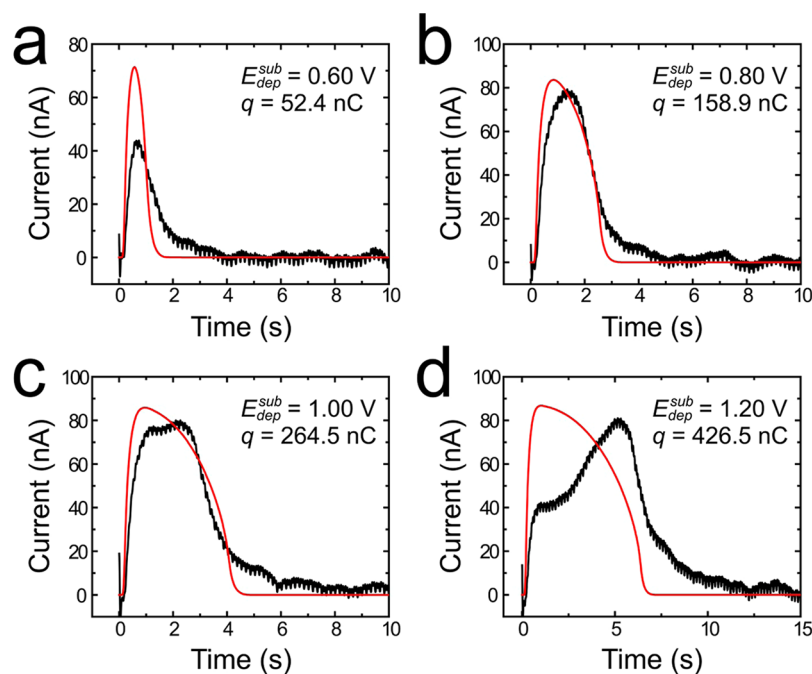
Figure 5. Experimental collector current transients (black) overlaid with finite-element simulation results (red). The values of E_{dep}^{sub} used to deposit the gold oxide are indicated in the legends. The solution contained 1.0 mM $K_3Fe(CN)_6$ and 0.10 M phosphate buffer (pH 7.0) flowing at $Q = 300$ nL min^{-1}. The experimental data were obtained using the same microelectrochemical device.

good. However, at very low and very high surface oxide concentrations there are significant disparities because of the sensitivity of the experiment and complex oxide phases, respectively.

There are a number of positive aspects of the types of results described herein. First, because the experiment operates within a microfluidic environment, there is excellent control over mass transfer, solution volumes are small, and applications to chemical sensing are easily envisioned. Second, there is flexibility in the size of the substrate being analyzed, and because the substrate is planar, chemical modification is straightforward. These factors should permit analysis of coatings having inherently low surface concentrations and those that are difficult to analyze directly on electrode surfaces (for example, membrane proteins constrained in lipid bilayers).

Despite these generally positive observations, there are also some problems with the implementation of the approach we describe. These include chemical interferences (i.e., Cl$^-$), the difficulty of finding an ideal redox titrant, and electrochemical interferences due to the oxygen permeability of PDMS. We plan to address these limitations, and report on other interesting types of surface-bound systems, in future studies.

◾ ASSOCIATED CONTENT

Ⓢ Supporting Information

Detailed description of device fabrication, average device measurements, experimental setup, graphical determination of t_{crit}, details from finite element simulations, and discussion of selection of redox probes. This material is available free of charge via the Internet at http://pubs.acs.org.

◾ AUTHOR INFORMATION

Corresponding Author
*E-mail: crooks@cm.utexas.edu.

◾ REFERENCES

(1) Compton, R. G.; Coles, B. A.; Fisher, A. C. *J. Phys. Chem.* **1994**, *98*, 2441−2445.
(2) Compton, R. G.; Coles, B. A.; Gooding, J. J.; Fisher, A. C.; Cox, T. I. *J. Phys. Chem.* **1994**, *98*, 2446−2451.
(3) Unwin, P. R.; Compton, R. G. In *Comprehensive Chemical Kinetics, v29: New Techniques for the Study of Electrodes and Their Reactions*; Elsevier: Amsterdam, 1989; pp 173−296.
(4) Amatore, C.; Da Mota, N.; Lemmer, C.; Pebay, C.; Sella, C.; Thouin, L. *Anal. Chem.* **2008**, *80*, 9483−9490.
(5) Fisher, A. C.; Compton, R. G. *J. Appl. Electrochem.* **1991**, *21*, 208−212.
(6) Unwin, P. R. *J. Electroanal. Chem. Interfacial. Electrochem.* **1991**, *297*, 103−124.
(7) Dumitrescu, I.; Yancey, D. F.; Crooks, R. M. *Lab Chip* **2012**, *12*, 986−993.
(8) Dumitrescu, I.; Crooks, R. M. *Proc. Natl. Acad. Sci. U. S. A.* **2012**, *109*, 11493−11497.
(9) Itagaki, M.; Suzuki, T.; Watanabe, K. *Electrochim. Acta* **1997**, *42*, 1081−1086.
(10) Sasaki, H.; Miyake, M.; Maeda, M. *J. Electrochem. Soc.* **2010**, *157*, E82−E87.
(11) Sasaki, H.; Maeda, M. *J. Electrochem. Soc.* **2010**, *157*, C414−C418.
(12) Shrestha, B. R.; Yadav, A. P.; Nishikata, A.; Tsuru, T. *Electrochim. Acta* **2011**, *56*, 9714−9720.

9968

dx.doi.org/10.1021/ac502869j | *Anal. Chem.* 2014, 86, 9962−9969

(13) Shrestha, B. R.; Nishikata, A.; Tsuru, T. *Electrochim. Acta* **2012**, *70*, 42−49.

(14) Sugawara, Y.; Okayasu, T.; Yadav, A. P.; Nishikata, A.; Tsuru, T. *J. Electrochem. Soc.* **2012**, *159*, F779−F786.

(15) Amatore, C.; Belotti, M.; Chen, Y.; Roy, E.; Sella, C.; Thouin, L. *J. Electroanal. Chem.* **2004**, *573*, 333−343.

(16) Amatore, C.; Oleinick, A.; Klymenko, O. V.; Svir, I. *ChemPhysChem* **2005**, *6*, 1581−1589.

(17) Amatore, C.; Oleinick, A.; Svir, I. *Electrochem. Commun.* **2004**, *6*, 1123−1130.

(18) Klymenko, O. V.; Oleinick, A. I.; Amatore, C.; Svir, I. *Electrochim. Acta* **2007**, *53*, 1100−1106.

(19) Rotating Ring-Disk Electrodes: MT28, MT29, E6, and E7 Series, Pine Instrument Company, Raleigh, NC, 27617.

(20) Amemiya, S.; Bard, A. J.; Fan, F.-R. F.; Mirkin, M. V.; Unwin, P. R. *Annu. Rev. Anal. Chem.* **2008**, *1*, 95−131.

(21) Xia, Y.; Whitesides, G. M. *Annu. Rev. Mater. Sci.* **1998**, *28*, 153−184.

(22) McDonald, J. C.; Duffy, D. C.; Anderson, J. R.; Chiu, D. T.; Wu, H.; Schueller, O. J. A.; Whitesides, G. M. *Electrophoresis* **2000**, *21*, 27−40.

(23) Qin, D.; Xia, Y.; Whitesides, G. M. *Nat. Protoc.* **2010**, *5*, 491−502.

(24) Bitziou, E.; Snowden, M. E.; Joseph, M. B.; Leigh, S. J.; Covington, J. A.; Macpherson, J. V.; Unwin, P. R. *J. Electroanal. Chem.* **2013**, *692*, 72−79.

(25) Bard, A. J.; Faulkner, L. R. *Electrochemical Methods: Fundamentals and Applications*, 2nd ed.; John Wiley & Sons: New York, 2001.

(26) Bard, A. J. In *Scanning Electrochemical Microscopy*, Bard, A. J.; Mirkin, M. V., Eds.; CRC Press: Boca Raton, FL, 2012; pp 1−14.

(27) Rodríguez-López, J.; Alpuche-Avilés, M. A.; Bard, A. J. *J. Am. Chem. Soc.* **2008**, *130*, 16985−16995.

(28) Rodríguez-López, J.; Minguzzi, A.; Bard, A. J. *J. Phys. Chem. C* **2010**, *114*, 18645−18655.

(29) Rodríguez-López, J.; Bard, A. J. *J. Am. Chem. Soc.* **2010**, *132*, 5121−5129.

(30) Zigah, D.; Rodríguez-López, J.; Bard, A. *J. Phys. Chem. Chem. Phys.* **2012**, *14*, 12764−12772.

(31) Park, H. S.; Leonard, K. C.; Bard, A. J. *J. Phys. Chem. C* **2013**, *117*, 12093−12102.

(32) Renault, C.; Anderson, M. J.; Crooks, R. M. *J. Am. Chem. Soc.* **2014**, *136*, 4616−4623.

(33) Yoo, J. J.; Anderson, M. J.; Alligrant, T. M.; Crooks, R. M. *Anal. Chem.* **2014**, *86*, 4302−4307.

(34) Amatore, C.; Da Mota, N.; Sella, C.; Thouin, L. *Anal. Chem.* **2007**, *79*, 8502−8510.

(35) Britz, D. *Digital Simulation in Electrochemistry*; Springer-Verlag: Berlin, 1988; p x.

(36) Oesch, U.; Janata, J. *Electrochim. Acta* **1983**, *28*, 1237−1246.